

# Robust Approach for Rotor Mapping in Cardiac Tissue

Daniel R. Gurevich<sup>1</sup> and Roman O. Grigoriev<sup>1</sup>

*School of Physics, Georgia Institute of Technology, Atlanta, GA 30332, USA*

(Dated: 30 July 2022)

The motion of and interaction between phase singularities that anchor spiral waves captures many qualitative and, in some cases, quantitative features of complex dynamics in excitable systems. Being able to accurately reconstruct their position is thus quite important, even if the data are noisy and sparse, as in electrophysiology studies of cardiac arrhythmias, for instance. A recently proposed global topological approach [Marcotte & Grigoriev, *Chaos* 27, 093936 (2017)] promises to dramatically improve the quality of the reconstruction compared with traditional, local approaches. Indeed, we found that this approach is capable of handling noise levels exceeding the range of the signal with minimal loss of accuracy. Moreover, it also works successfully with data sampled on sparse grids with spacing comparable to the mean separation between the phase singularities for complex patterns featuring multiple interacting spiral waves.

Keywords: phase singularity, cardiac arrhythmia, spiral wave chaos

**Catheter ablation has recently emerged as a leading surgical treatment for a range of cardiac arrhythmias, especially atrial fibrillation. The premise of the treatment is that certain localized regions of heart tissue can become sources of spiral excitation waves – or rotors – competing with the heart’s natural pacemaker, i.e., the sinoatrial node for the atria or the atrio-ventricular node for the ventricles. The success of the surgery then critically depends on the precision with which these sources are located in preparation for surgery based on electrograms obtained using intra-cardiac multi-electrode catheters. This paper explains how the sources of the excitation waves can be reliably located with subgrid precision using such sparse and noisy measurements of the transmembrane voltage.**

## I. INTRODUCTION

Spiral waves in two dimensions (and scroll waves in three dimensions) represent the key motifs of typical self-sustained dynamical patterns in excitable systems such as cardiac tissue. In fact, the work to understand the mechanisms and develop effective treatments of cardiac arrhythmias such as tachycardia or fibrillation became the major driver for much of the recent interest in the dynamics of spiral and scroll waves. Because of the strong spatial coherence of such waves, many aspects of their dynamics can in fact be understood using center manifold reduction of the underlying partial differential (or difference) equations, yielding a system of ordinary differential equations with respect to just a few variables<sup>1,2</sup>. These variables are associated with the Euclidean symmetry of the problem and can be interpreted in terms of the low-dimensional dynamics (translation and rotation) of the core of the spiral wave, which serves as its source and anchor. Notable examples include meander and drift<sup>3–6</sup> of spiral waves and their interaction with boundaries<sup>7–9</sup>.

In fact, even for complex patterns of excitation which involve multiple spiral waves, many features of the dynamics can be understood and described reasonably well in terms of the wave core interaction<sup>9,10</sup>.

Given their influence on large regions of space, spiral wave cores represent attractive targets for controlling the dynamics of excitable media. This is well-known to clinical practitioners looking for treatments of cardiac arrhythmias such as atrial fibrillation. In fact, radio frequency ablation, which aims to silence regions of cardiac tissue believed to be sources of spiral excitation waves (often referred to as rotors), has become the leading surgical treatment for persistent atrial fibrillation<sup>11,12</sup>. The success rate of ablation surgeries is however not very high, suggesting that the accuracy with which the spiral wave cores are located is insufficient. Indeed, typical intra-cardiac basket catheters used to locate them only have 64 unipolar electrodes distributed over 8 circular spines of the catheter<sup>13</sup>. The signal they generate is both rather sparse and rather noisy, making it challenging to identify the location of the spiral wave cores, especially if those cores are drifting or meandering.

This paper describes a novel method that can reliably identify and track with high precision a large number of spiral wave cores based on sparse and noisy measurements of the transmembrane voltage. The paper is organized as follows. An overview of the existing methods for identifying the cores (or, more precisely, certain points inside the cores) is provided in Section II. Our approach is described in Section III, and it is validated and compared with competing approaches in Section IV. Finally, our conclusions are presented in Section V.

## II. BACKGROUND

Spiral wave cores tend to be exponentially localized, as illustrated by analyses of the Ginzburg-Landau<sup>14</sup>, Barkley<sup>15</sup>, FitzHugh-Nagumo<sup>16</sup>, Oregonator<sup>17</sup>, Beeler-Reuter-Pumir<sup>18</sup>, and Karma<sup>9</sup> models. In practice, it is more convenient to define a single point that character-

izes the position of the core. Numerical studies tend to use the position of the spiral tip, which can be defined in many different ways<sup>10,19–30</sup>. The most popular definitions are based on either the intersection of level sets of different variables<sup>22</sup> or the vanishing of the normal velocity<sup>24</sup> or the curvature of the wavefront<sup>29</sup>.

Neither of these definitions are convenient (or reliable) for analyzing experimental data, however. An alternative approach relies on the phase-amplitude representation of spiral waves<sup>31</sup>, with the phase singularity (PS) defining the instantaneous center of rotation of the wave. A method for identifying PSs based on the local phase field has become standard in analyzing experimental data<sup>26,32</sup>, although it is also possible to determine the location of PSs using the amplitude field<sup>10</sup>.

Recently, several alternative approaches have been proposed to locate spiral wave cores based on various metrics such as Shannon entropy, multi-scale frequency, kurtosis, multi-scale entropy<sup>33</sup>, and Jacobian determinant<sup>34</sup>. It should be noted that these metrics define neither the spiral tip nor the phase singularity, but they can be applied to sparse data, although their precision and accuracy decrease very quickly as sparsity increases. The study of Li *et al.*<sup>34</sup> showed that the accuracy and precision of the Jacobian determinant method is superior to that of other common approaches for both stationary and meandering spirals. Furthermore, they determined that the Jacobian determinant method is the only one that can produce reliable results in the presence of as little as 0.9% noise.

In fact, essentially all existing methods for locating spiral wave cores are local and cannot withstand higher noise levels characteristic of practical applications without significant loss of accuracy and precision. The only exception is the global topological method for identifying PSs proposed by Marcotte and Grigoriev<sup>35</sup>. The original version of the topological approach defined PSs as intersections of level sets associated with two different variables (one fast, one slow). A modified version of this topological approach based on phase reconstruction that required measurement of just one variable was developed and tested using spatially resolved numerical and experimental data<sup>36</sup>. Here we describe a more robust implementation of the topological approach that does not require phase reconstruction and investigate its performance for sparse and noisy data generated by a model of atrial fibrillation.

### III. METHODS

#### A. Model

To illustrate the algorithm and determine the conditions under which it functions reliably, we will use two-dimensional surrogate data generated by the smoothed version of the Karma model<sup>37,38</sup>,

$$\partial_t \mathbf{w} = D \nabla^2 \mathbf{w} + \mathbf{f}(\mathbf{w}), \quad (1)$$

where  $\mathbf{w} = [u, v]$ ,  $u$  is the (fast) voltage variable,  $v$  is the (slow) gating variable,

$$\begin{aligned} f_1 &= (u^* - v^M) \{1 - \tanh(u - 3)\} u^2 / 2 - u, \\ f_2 &= \epsilon \{ \beta \Theta_s(u - 1) + \Theta_s(v - 1)(v - 1) - v \}, \end{aligned} \quad (2)$$

and  $\Theta_s(u) = [1 + \tanh(su)]/2$ . Here  $\epsilon$  describes the ratio of the fast and slow time scales,  $s$  is the smoothing parameter, and the diagonal matrix  $D$  of diffusion coefficients describes the spatial coupling between neighboring cardiac cells (cardiomyocytes). The parameters of the model are  $M = 4$ ,  $\epsilon = 0.01$ ,  $s = 10$ ,  $\beta = 1.389$ ,  $u^* = 1.5415$ ,  $D_{11} = 4.0062$ , and  $D_{22} = 0.20031$ , with the length scale corresponding to the size of a cardiomyocyte. Along with the Mitchell-Schaeffer model<sup>39</sup>, this is one of the simplest models of cardiac tissue that develops sustained spiral wave chaos from an isolated spiral wave through the amplification of the alternans instability.

#### B. Analysis

The method described here can in principle be used to reconstruct the position and dynamics of PSs using any spatially and temporally resolved scalar field; in this study we chose the voltage variable  $u$  (normalized to the range  $[0, 1]$  for convenience). In some instances, e.g., electrophysiology studies using basket catheters, the data are only available on a coarse spatial grid. To enable rotor mapping with meaningful accuracy in such cases, the data at each frame of the recording are mapped onto a sufficiently fine mesh using bicubic interpolation.

Following the original study that introduced the topological approach<sup>35</sup>, we will define PSs as the intersections of two level sets, one describing the boundary of the excited region  $E$  and the other describing the boundary of the refractory region  $R$ . In particular,

$$R = \{(x, y) : \dot{u} < 0\}. \quad (3)$$

In the original study, the excited region  $E$  was defined using the temporal derivative of an independent field (gating variable). Since we assume no other fields can be measured, we define the excited region in terms of  $\ddot{u}$ :

$$E = \{(x, y) : \ddot{u} < 0\}. \quad (4)$$

For stationary spirals, the details of this choice are not important and both definitions produce the same result. Each PS therefore lies at the intersection of two level sets:

$$\begin{aligned} \partial R &= \{(x, y) : \dot{u} = 0\}, \\ \partial E &= \{(x, y) : \ddot{u} = 0\}. \end{aligned} \quad (5)$$

Given that our data are discrete and noisy, properly defining the level sets and PSs requires more care.

In this study, both temporal derivatives of  $u$  were computed using finite differencing, although other methods could be used as well. In the presence of noise (i.e., when

processing experimental recordings),  $u(x, y, t)$  may initially be smoothed using a Gaussian kernel with spatial and temporal widths  $\sigma_s$  and  $\sigma_t$ , respectively. At each frame, we will redefine  $\partial R$  and  $\partial E$  as the sets of grid points that are either peaks or troughs of the time series of  $u$  and  $\dot{u}$ , respectively. Even after smoothing,  $u$  and especially  $\dot{u}$  can remain noisy, so each peak or trough is required to have a minimum prominence (a fraction  $MPP_1$  or  $MPP_2$  of the range of  $u$  or  $\dot{u}$ , respectively, selected based on the overall level of noise) and separation (generally a fixed fraction  $\delta$  of the dominant period of oscillation) from the nearest peak/trough.

Even after this processing, the local definition of the level sets  $\partial R$  and  $\partial E$  can remain sensitive to noise, however. Furthermore, spatial discreteness of the data – we assume  $u$  is measured on a uniform grid  $(x_i, y_j, t_n)$  in space and time – also limits the accuracy with which the level sets can be defined. Let  $t_{ijm}^1$  denote the position of subsequent peaks (troughs) of  $u(x_i, y_j, t)$  for  $m$  even (odd), and define  $t_{ijm}^2$  analogously for  $\dot{u}(x_i, y_j, t)$ . Further, let us define a noise-insensitive analog of the sign of the time derivative

$$s_{ijn}^k = \begin{cases} 1, & t_{ijm-1}^k < t_n \leq t_{ijm}^k \\ -1, & t_{ijm}^k < t_n \leq t_{ijm+1}^k \end{cases} \quad (6)$$

for some even number  $m$  and  $k = 1$  or  $2$ . Then the sets

$$\ell^k(t_n) = \{(x_i, y_j) : \exists i', j' : s_{ijn}^k s_{i'j'n}^k < 0, \\ |i - i'| + |j - j'| = 1\} \quad (7)$$

are discrete generalizations of the level sets  $\partial R$  and  $\partial E$  with a minimal width of 2 grid points and no gaps.

In order to define the position of the level sets with sub-grid precision using global, rather than local (and hence noisy), information, we use the following approach. For each of  $\ell^1$  and  $\ell^2$ , unsigned distance functions  $d^1$  and  $d^2$ , respectively, are constructed using the MATLAB function `bwdist`<sup>40</sup>. These are in turn converted into signed distance functions:

$$d_s^k(x_i, y_j, t_n) = -s_{ijn}^k d^k(x_i, y_j, t_n), \quad (8)$$

where in the following discussion we will drop the explicit dependence on  $t_n$ . Next, in order to ultimately smooth the level sets, a spatial convolution of the signed distance functions with a Gaussian kernel with spatial width  $\sigma_d$  is computed, yielding a pair of smoothed distance fields  $\bar{d}_s^k$  which incorporate global information across the entire domain. A comparison of the smoothed and unsmoothed versions of the signed distance function is presented in Fig. 1. Note the plateaus in the unsmoothed distance function, representing the finite thickness of the set from which it is computed.

Now we can finally define curves  $\bar{\ell}^k$  as the zero level sets of the smoothed distance fields  $\bar{d}_s^k$  using the MATLAB function `contour`. These curves are piecewise continuous and smooth, although in practice they are parametrized by a sequence of connected points in  $\mathbb{R}^2$ . Note that  $\ell_k$

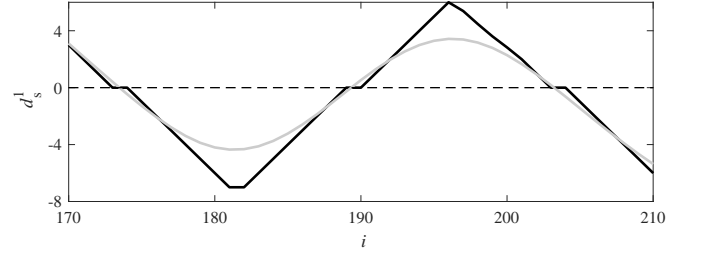


FIG. 1. The signed distance  $d_s^1$  (black) and its smoothed version  $\bar{d}_s^1$  (gray) at a fixed time over a  $j = \text{const}$  slice of the domain.

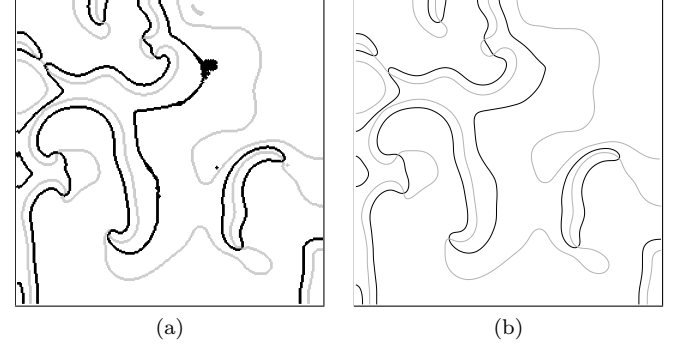


FIG. 2. Comparison of sets  $\ell^k$  (a) and  $\bar{\ell}^k$  (b) for noiseless data, with  $k = 1$  in black and  $k = 2$  in gray. The domain is  $256 \times 256$  grid points. Panel (a) contains a number of artifacts, which have to do with a characteristic feature of most cardiac models, namely very flat repolarization plateaus.

define the true positions of  $\partial R$  and  $\partial E$  with a precision of one grid point. As Fig. 2 illustrates, for noiseless data,  $\bar{\ell}^k$  provide accurate representations of  $\ell^k$  and hence  $\partial R$  and  $\partial E$ , despite the relatively aggressive smoothing.

We will determine PSs as the intersections of  $\bar{\ell}^1$  and  $\bar{\ell}^2$ , which are computed with sub-grid precision using the MATLAB function `intersections`<sup>41</sup>. The chirality (or topological charge)  $q$  of each PS can be computed using the gradients of  $\bar{d}_s^1$  and  $\bar{d}_s^2$ , which are nearly constant in the vicinity of a PS, as follows:

$$q = \text{sign}(\hat{\mathbf{z}} \cdot \nabla \bar{d}_s^1 \times \nabla \bar{d}_s^2), \quad (9)$$

These gradients are approximated at the four grid points nearest to the PS using finite differencing and then interpolated to the exact location of the PS. This interpolation can be essential to correctly determine the chiralities of a pair of phase singularities separated by only a few grid points (in practice, as few as one).

Chirality plays an important role in the topological analysis of the excitation patterns produced during arrhythmias<sup>35</sup>. It is also useful for reconstructing PS trajectories, which are computed using a MATLAB implementation<sup>42</sup> of the IDL particle tracking method<sup>43</sup>, with the positions and chiralities of all PSs found at each time step as input parameters. Both experimental and

numerical data feature many short trajectories that correspond to virtual spiral waves that exist for a fraction of a rotation period. Such structures do not appear to play a dynamically important role, so in our analysis we ignore PSs with lifetimes shorter than the dominant period of oscillation. For comparison, during electrophysiological studies in a clinical setting, only spiral waves that persist for at least two rotations are considered<sup>44</sup>.

#### IV. RESULTS

To test the algorithm, we generated 4000 frames of surrogate data (after discarding 600 frames representing the initial transient) separated by one time unit by numerically integrating the model described above on a square domain of size  $256 \times 256$  with no-flux boundary conditions. This can be considered a fine mesh as it fully resolves all of the spatial features of the solution. In our units, the typical rotation period of a spiral wave is  $T = 53$ , the mean separation between PSs is  $L = 46$ , and the mean number of PSs is 12.7.

##### A. Benchmark

In order to establish a benchmark for quantifying how our approach copes with noise and data sparsity, we analyzed the data using a parameter set representing minimal smoothing (cf. Appendix A). Fig. 3 presents six equally spaced snapshots of the benchmark (voltage) data over roughly a rotation period. Superimposed are the curves  $\bar{\ell}^1$  (the boundary of the refractory region, in white) and  $\bar{\ell}^2$  (the boundary of the excited region, in black). The intersections define PSs (black/white circles for positive/negative chirality).

Many spiral waves are seen to rotate stably around fixed or weakly meandering PSs. The trajectories of the long-lived PSs are shown over the same interval in Fig. 4, with the thicker curves corresponding to PSs created during this time. Three different PS pair creation events are visible during this period: one between snapshots (b) and (c) near the left edge of the domain, and two between snapshots (e) and (f) near the left and right edges.

Notably, the lone thick blue trajectory in Fig. 4 appears to be missing its opposite chirality counterpart. In fact, that counterpart is not shown since it corresponds to a short-lived “virtual” PS which annihilates with a nearby long-lived PS soon after the last frame in Fig. 3. Note that the trajectories of created PS pairs do not start at the exact same point because of the finite temporal resolution of the data. When the PSs are created and destroyed, they move especially quickly, separating by several grid spacings in one time unit. Much higher temporal resolution is needed to resolve the fast motion of PSs during pair creation/annihilation events.

The ability of our algorithm to automatically track PSs (both short- and long-lived) allows one to generate statis-

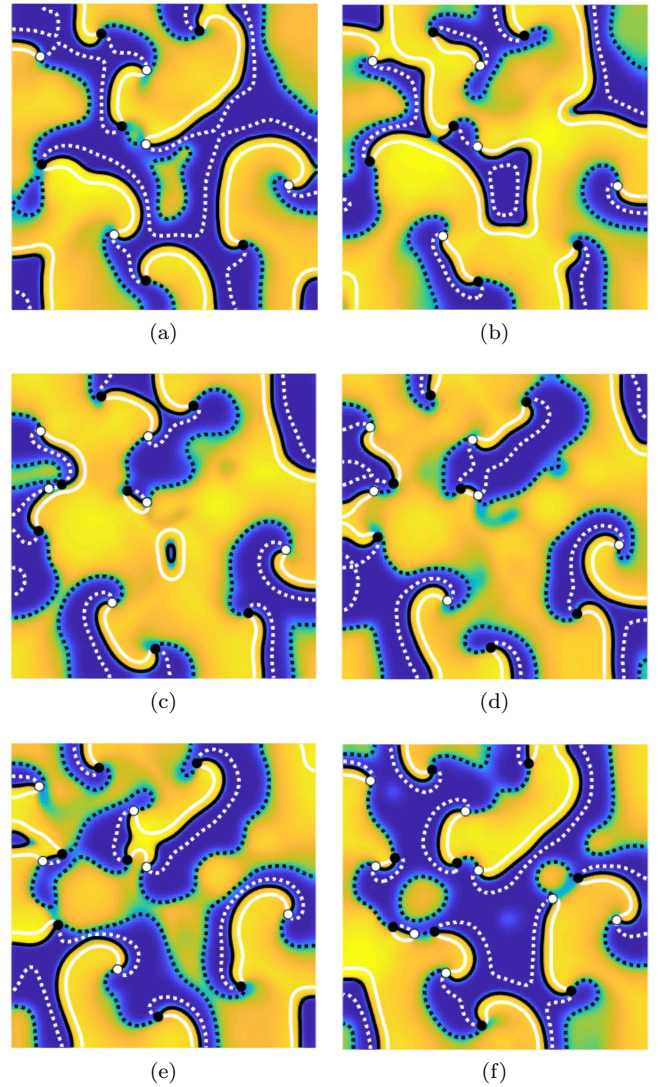


FIG. 3. Snapshots of benchmark data (colorbar is shown in Fig. 6(a)) equally spaced in time over 56 frames (approximately one rotation period), with curves  $\bar{\ell}^1$  (white) and  $\bar{\ell}^2$  (black) and PSs superimposed. Here and below, solid and dashed white segments correspond to the leading and trailing edges of the refractory region, respectively; solid and dashed black correspond to the wavefront and waveback. PSs with chirality +1 and -1 are respectively shown as black and white circles. The  $x$  ( $y$ ) axis is horizontal (vertical). A full movie is provided in the supplementary material.

tics that could be extremely useful (e.g., for model validation) but would be hard to obtain otherwise. To illustrate this, Fig. 5 shows various PS statistics (only taking spiral waves that complete at least one revolution into account) over the course of the entire simulation. In particular, we find that the number of PSs ranges rather widely (between 5 and 20, as shown in panel (a)). This illustrates that our approach can easily and reliably identify at least 20 PSs simultaneously, which is far more than any existing alternative. The distances between PSs also

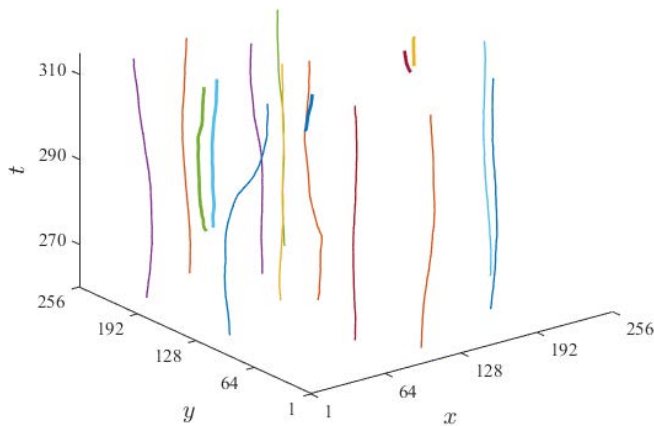


FIG. 4. Trajectories of PSs with lifetimes of at least one period during the same time interval as shown in Fig. 3. Thicker curves correspond to PSs created during this period.

vary rather significantly, with a pronounced peak at 46 units (panel (b)). As we will show below, it is this characteristic length scale, not the wavelength of the pattern (91 units here), that determines the sparsity at which our method starts to break down.

We find that while the majority of spiral waves are relatively short lived (panel (c)), some can live for up to 45 periods (for reference, the duration of the entire data set corresponds to 75 periods). Such instances of functional reentry could easily be mistaken for structural reentry in a clinical setting. In light of this “longevity,” it is perhaps not surprising that some PSs drift over distances exceeding half the size of our rather large system (panel (d)). While the lifetime and drift statistics of PSs in the Karma model may not be particularly relevant for atrial fibrillation, a similar analysis of data from basket catheters could yield a treasure trove of clinically valuable information.

## B. Sensitivity to noise and sparsification

To represent the effect of imperfections in realistic experimental recordings, noisy data sets were produced by adding random Gaussian-distributed white noise with some standard deviation  $\eta$  to the benchmark data. In addition, sparsified data were generated by sampling from the benchmark or noisy data on a uniform grid with lower resolution by a factor of  $2^n$  in each spatial dimension for some integer  $n > 1$ . The sparsified data was then interpolated back onto the original grid for processing.

For all noise and sparsity levels, the resulting data were processed using modified parameter sets mildly optimized to deal with high levels of noise (cf. Appendix A). Note that, in order to preserve precision when the data are sparse, no initial spatial smoothing is applied. The robustness of the algorithm is thus ensured without relying on averaging of high-spatial-resolution data to counteract the effects of noise. As we show below, our

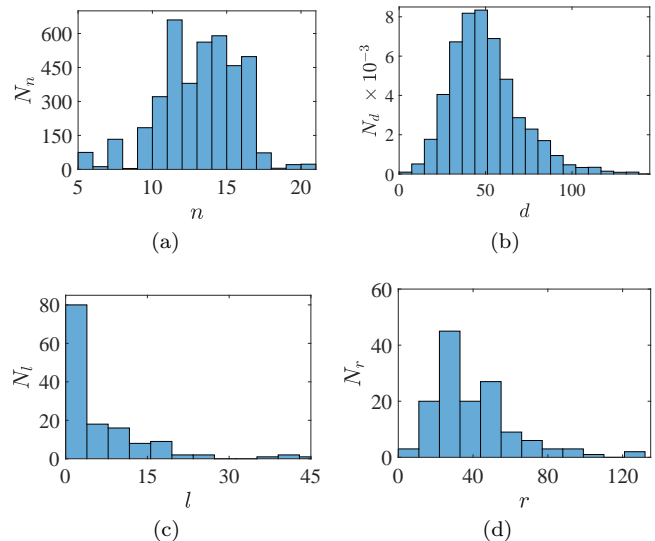


FIG. 5. PS statistics. (a) Histogram of the total number  $n$  of PSs in each frame. (b) Histogram of the distance  $d$  from each PS to the nearest PS of opposite chirality, computed separately for each PS in each frame. (c) Histogram of the lifetime  $l$  in periods of each PS. (d) Histogram of the separation  $r$  between the most distant pair of points along the trajectory of each PS.

results are extremely robust to both noise and sparsification but show some minor reduction in precision of PS location, even for the benchmark data.

The effect of noise alone on the performance of the algorithm is illustrated in Fig. 6, which shows the level sets  $\bar{\ell}^1$ ,  $\bar{\ell}^2$ , and the PSs computed for the same frame with four levels of noise ( $\eta = 0, 0.1, 0.3, 1$ ). As the data quality deteriorates, the computed curves, especially  $\bar{\ell}^1$ , become increasingly unreliable; it is impossible to filter out all false peaks in the data without ignoring the smaller but legitimate and dynamically important fluctuations in voltage. Nevertheless, their intersections (the PSs) are located with high precision in all cases, even when  $\eta$  is as large as the entire range of the original data.

Similarly, the effect of sparsity alone is illustrated in Fig. 7, which shows the same frame with (noiseless) data interpolated from coarse grids with four different spatial resolutions: (a)  $256 \times 256$ , (b)  $32 \times 32$ , (c)  $16 \times 16$ , (d)  $8 \times 8$ . For resolutions down to  $16 \times 16$ , the computed level sets are qualitatively very similar to the benchmark and all long-lived PSs are correctly detected and located with precision substantially better than the coarse grid spacing. In the  $16 \times 16$  snapshot, there is a pair of virtual PSs in the lower left corner that are not present in the benchmark analysis. These are short-lived and so are discarded in our analysis. Even for data on an  $8 \times 8$  spatial grid, a large fraction of PSs were correctly identified, with one false positive; the error in the position of the correct PSs is substantially smaller than  $256/8 = 32$  units. However, it is apparent that many of the dynamical features cannot be properly resolved when the grid

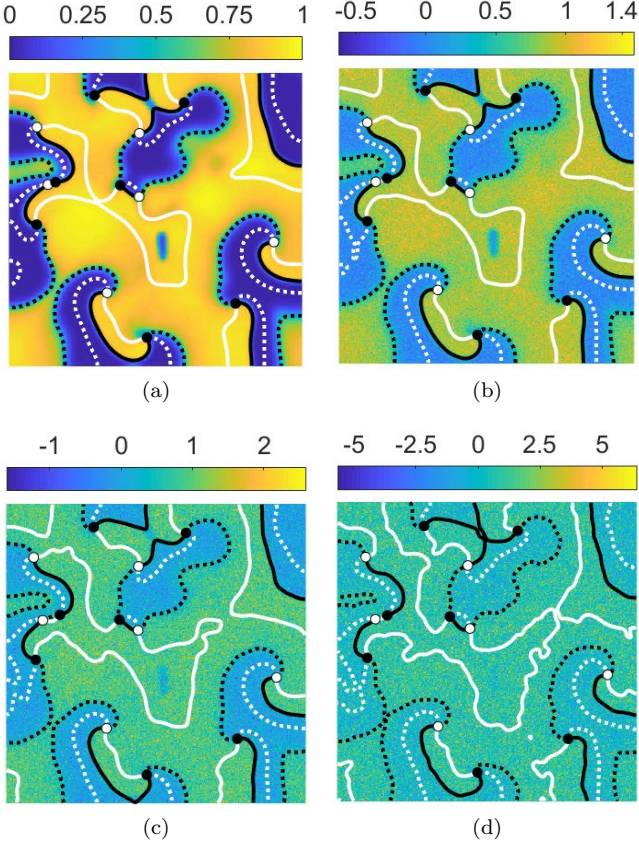


FIG. 6. The frame shown in Fig. 3(c) with four different levels of added noise ( $\eta = 0, 0.1, 0.3, 1$ ); overlaid are the curves  $\ell^1$  and  $\ell^2$  and PSs computed from the noisy data in each case.

resolution becomes comparable to the mean separation between PSs.

Tables I and II quantify the accuracy and precision of the algorithm in the presence of both noise and sparsity. In the following discussion, we will use the benchmark analysis as the reference. For each level of noise and sparsity, we compare the computed trajectories with the reference trajectories as follows. At each frame, every PS is matched with the nearest reference PS of the same chirality, provided that their separation is no greater than a fixed fraction  $\alpha$  of the mean PS separation  $L$ . Each PS trajectory is then paired with all reference PS trajectories with which it was matched for at least a given fraction  $\gamma$

	$256 \times 256$	$64 \times 64$	$32 \times 32$	$16 \times 16$	$8 \times 8$
$\eta = 0$	0.995	0.995	0.994	0.955	0.255
$\eta = 0.1$	0.993	0.994	0.992	0.957	0.308
$\eta = 0.3$	0.988	0.988	0.985	0.954	0.357
$\eta = 1$	0.990	0.974	0.849	0.695	-

TABLE I. PS detection accuracy  $\rho_t$  as a function of sparsity and noise level  $\eta$ . The quality of the analysis was too poor to compute trajectories when both sparsity and noise were maximal.

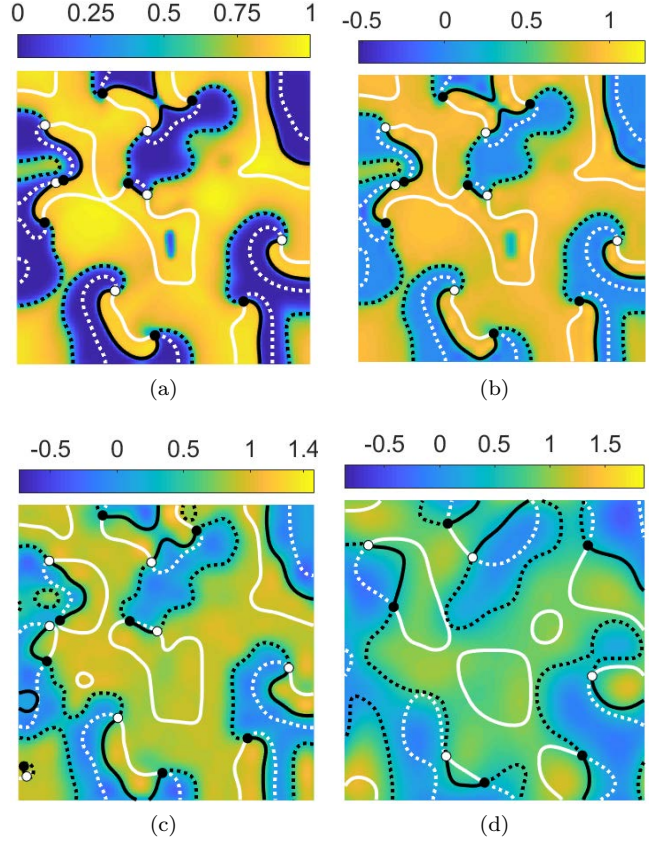


FIG. 7. The frame shown in Fig. 3(c) after interpolating from four levels of sparsification: (a) spatial resolution  $256 \times 256$  (same as benchmark), (b)  $32 \times 32$ , (c)  $16 \times 16$ , (d)  $8 \times 8$ . As in the previous figure, the curves  $\ell^1$  and  $\ell^2$  and PSs computed from the sparsified data are overlaid.

	$256 \times 256$	$64 \times 64$	$32 \times 32$	$16 \times 16$	$8 \times 8$
$\eta = 0$	1.1	1.1	1.4	4.8	9.9
$\eta = 0.1$	1.2	1.3	1.6	4.6	9.6
$\eta = 0.3$	1.7	1.8	2.3	4.9	9.4
$\eta = 1$	2.3	3.1	4.5	6.9	-

TABLE II. PS location precision  $\rho_d$  (in units of the fine mesh) as a function of sparsity and noise level  $\eta$ .

of the period  $T$ , with all other matches discarded. (We allow for a trajectory to be matched to multiple other trajectories to account for the possibility that some trajectories might be broken up by short gaps.) Finally, we compute  $\rho_d$ , the average distance between the detected and reference PS across all matches, as well as the ratio

$$\rho_t = \frac{2 \sum_t m_t}{\sum_t (r_t + n_t)} \quad (10)$$

where the sum is over all frames and  $m_t$ ,  $r_t$ , and  $n_t$  are the number of matches, reference PSs, and detected PSs, respectively, in frame  $t$ ;  $\rho_t$  ranges from 0 to 1 and represents the PS detection accuracy. The results in the tables summarize the results for all data sets using fairly

strict parameter choices  $\alpha = 0.35$  and  $\gamma = 0.8$ . (For our surrogate data, this means two trajectories are matched only if their separation is at most 16 units for at least 43 frames.)

The performance of the algorithm was extremely good in a wide range of conditions. Note that the accuracy and precision is imperfect even in the case of full resolution and no noise; this is because of the temporal smoothing used in this analysis, which is not present in the benchmark. PS detection accuracy is above 98%, with precision of about 5% of the mean PS separation or better, for 10 out of the 20 data sets, even in one case when  $\eta = 1$ . (When the accuracy is close to 100%, most of the mismatches are due to PS pair creation or annihilation events being detected a few frames earlier or later than in the reference analysis, an error that has little to no dynamical importance.) In most of the  $16 \times 16$  data sets, for which the coarse grid resolution is approximately equal to  $\alpha L$ , the accuracy remains above 95% and the precision is better than 5 spatial units (i.e., about 1 mm), demonstrating that the algorithm can locate PSs with sub-grid precision. The analysis only breaks down for data sampled on  $8 \times 8$  grids, which is near the theoretical limit of such a method as the grid spacing (32 units) is comparable to the mean PS separation (46 units).

### C. Comparison with alternative approaches

To validate our algorithm, we also implemented and tested its most robust alternative, the Jacobian determinant method<sup>34</sup>. The method essentially identifies PSs with the extrema of the two-dimensional field

$$\mathcal{D}(t) = \left| \begin{array}{cc} \frac{\partial u}{\partial x} \Big|_t & \frac{\partial u}{\partial y} \Big|_t \\ \frac{\partial u}{\partial x} \Big|_{t+\tau} & \frac{\partial u}{\partial y} \Big|_{t+\tau} \end{array} \right| = \hat{z} \cdot (\nabla u|_t \times \nabla u|_{t+\tau}), \quad (11)$$

where  $\tau$  is an empirically chosen time delay. This method was used to compute PS trajectories for the full resolution ( $256 \times 256$ ) data sets with varying levels of noise, and the results were compared to our benchmark analysis. The time delay parameter was chosen to be  $\tau = 0.1125T = 6$  frames, which is approximately the value found to work best in the original paper. Like our method, the Jacobian determinant method is better suited than traditional techniques to the presence of non-stationary PSs, noise, and/or sparsity. However, we observed some difficulties not present in our approach.

First, the extrema of the field  $\mathcal{D}$  must be defined with care as the less pronounced peaks do not correspond to PSs. As a result, some minimum peak prominence must be selected on a case-by-case basis for each recording and it is unclear how to determine the optimal choice without a reference. Such an approach may not be feasible for experimental recordings, especially in the presence of spatial heterogeneity, which might cause the optimal threshold to vary in space. For our data, we obtained the highest accuracy when labeling as PSs all extrema with a

	$\eta = 0$	$\eta = 0.1$	$\eta = 0.3$	$\eta = 1$
$\rho_t$	0.969	0.956	0.895	-
$\rho_d$	1.7	1.7	1.7	-

TABLE III. PS detection accuracy  $\rho_t$  and precision  $\rho_d$  for the Jacobian determinant method as a function of noise level  $\eta$ . Analysis quality was too poor to compute trajectories for  $\eta = 1$ .

prominence exceeding the maximum value of  $|\mathcal{D}|/3$ . Second, even in the absence of noise, some peaks corresponding to a single non-stationary PS were found to separate into multiple local extrema of similar magnitude, making it difficult to determine the exact number of PSs and their locations. Finally, spatial smoothing of  $\mathcal{D}$  was necessary to eliminate spurious PSs for  $\eta$  as small as 0.1 (the lowest noise level we tested). This step substantially reduces precision of PS location when the data are both noisy and sparse.

We smoothed  $\mathcal{D}$  using a Gaussian kernel with a width of 2 grid spacings, which is in close correspondence with the authors' suggested approach. In fact, this substantially improved accuracy even in the absence of noise, likely because of the second difficulty mentioned previously. The results of the comparison of the smoothed Jacobian determinant method with the benchmark are summarized in Table III. The Jacobian determinant method performed very well for  $\eta \leq 0.1$ , achieving over 95% accuracy, but accuracy fell below 90% at  $\eta = 0.3$ , and for  $\eta = 1$  no meaningful results could be produced as some frames contained over 100 spurious PSs. This comparison demonstrates that the Jacobian determinant method can handle moderate levels of noise but falls apart at the higher noise levels that can be easily handled by our algorithm. Our approach is also superior in handling sparse data as it locates PSs with resolution much better than the resolution of the coarse grid.

## V. CONCLUSIONS

We have introduced a novel approach for identifying the locations of multiple phase singularities associated with complicated patterns of excitation waves based on measurements of a single scalar field. Because of its global nature, the new method was found to be substantially more robust than any previous, essentially local, methods aimed at identifying “organizing centers” of spiral wave activity. In particular, we have demonstrated that our approach can simultaneously identify and locate tens of phase singularities, including ones that are highly nonstationary. Moreover, their locations can be tracked in time with subgrid precision for data that are both very noisy (with noise level exceeding the signal level) and very sparse (on grids with spacing comparable to the mean separation between phase singularities). This enables collection of a wide range of statistical information that can be used in model validation, for instance, and

promises to make a large impact on applications such as clinical electrophysiology studies using intra-cardiac multi-electrode basket catheters. It is worth emphasizing, however, that this method is not restricted to cardiac tissue and can be applied to any two-dimensional excitable system. Extensions to three dimensions are possible as well but are outside of the scope of this paper.

## SUPPLEMENTARY MATERIAL

A movie showing the dynamics of PSs and the level sets corresponding to the wavefronts, wavebacks, and the leading/trailing edges of the refractory region in the benchmark analysis is provided as supplementary material.

## ACKNOWLEDGMENTS

DG gratefully acknowledges the support of the GT College of Sciences Undergraduate Research Science Award and NSF Award Number 1446675.

## VI. REFERENCES

- <sup>1</sup>D. Barkley, “Euclidean symmetry and the dynamics of rotating spiral waves,” *Phys. Rev. Lett.* **72**, 164–167 (1994).
- <sup>2</sup>B. Sandstede, A. Scheel, and C. Wulff, “Dynamics of spiral waves on unbounded domains using center-manifold reductions,” *Journal of differential equations* **141**, 122–149 (1997).
- <sup>3</sup>V. N. Biktashev and A. V. Holden, “Resonant drift of autowave vortices in two dimensions and the effects of boundaries and inhomogeneities,” *Chaos Soliton Fract.* **5**, 575–622 (1995).
- <sup>4</sup>V. N. Biktashev, A. V. Holden, and E. V. Nikolaev, “Spiral wave meander and symmetry of the plane,” *Int. J. Bifur. Chaos* **6**, 2433–2440 (1996).
- <sup>5</sup>B. Fiedler, B. Sandstede, A. Scheel, and C. Wulff, “Bifurcation from relative equilibria of noncompact group actions: Skew products, meanders, and drifts,” *Doc. Math.* **141**, 479–505 (1996).
- <sup>6</sup>B. Fiedler and D. Turaev, “Normal forms, resonances, and meandering tip motions near relative equilibria of Euclidean group actions,” *Arch. Rational Mech. Anal.* **145**, 129–159 (1998).
- <sup>7</sup>J. Langham and D. Barkley, “Non-specular reflections in a macroscopic system with wave-particle duality: Spiral waves in bounded media,” *Chaos* **23**, 013134 (2013).
- <sup>8</sup>J. Langham, I. Biktasheva, and D. Barkley, “Asymptotic dynamics of reflecting spiral waves,” *Phys. Rev. E* **90**, 062902 (2014).
- <sup>9</sup>C. D. Marcotte and R. O. Grigoriev, “Adjoint eigenfunctions of temporally recurrent single-spiral solutions in a simple model of atrial fibrillation,” *Chaos* **26**, 093107 (2016).
- <sup>10</sup>G. Byrne, C. D. Marcotte, and R. O. Grigoriev, “Exact coherent structures and chaotic dynamics in a model of cardiac tissue,” *Chaos* **25**, 033108 (2015).
- <sup>11</sup>S. M. Narayan, D. E. Krummen, K. Shivkumar, P. Clopton, W.-J. Rappel, and J. M. Miller, “Treatment of atrial fibrillation by the ablation of localized sources: CONFIRM (Conventional Ablation for Atrial Fibrillation With or Without Focal Impulse and Rotor Modulation) trial,” *Journal of the American College of Cardiology* **60**, 628–636 (2012).
- <sup>12</sup>K. Shivkumar, K. A. Ellenbogen, J. D. Hummel, J. M. Miller, and J. S. Steinberg, “Acute termination of human atrial fibrillation by identification and catheter ablation of localized rotors and sources: first multicenter experience of focal impulse and rotor modulation (FIRM) ablation,” *Journal of cardiovascular electrophysiology* **23**, 1277–1285 (2012).
- <sup>13</sup>J. Laughner, S. Shome, N. Child, A. Shuros, P. Neuzil, J. Gill, and M. Wright, “Practical considerations of mapping persistent atrial fibrillation with whole-chamber basket catheters,” *JACC: Clinical Electrophysiology* **2**, 55–65 (2016).
- <sup>14</sup>I. V. Biktasheva and V. N. Biktashev, “Response functions of spiral wave solutions of the complex Ginzburg-Landau equation,” *J. Nonlin. Math. Phys.* **8**, 28–34 (2001).
- <sup>15</sup>H. Henry and V. Hakim, “Scroll waves in isotropic excitable media: Linear instabilities, bifurcations, and restabilized states,” *Phys. Rev. E* **65**, 046235 (2002).
- <sup>16</sup>I. V. Biktasheva, A. V. Holden, and V. N. Biktashev, “Localization of response functions of spiral waves in the FitzHugh-Nagumo system,” *Int. J. Bifur. Chaos* **16**, 1547–1555 (2006).
- <sup>17</sup>I. V. Biktasheva, H. Dierckx, and V. N. Biktashev, “Drift of scroll waves in thin layers caused by thickness features: Asymptotic theory and numerical simulations,” *Phys. Rev. Lett.* **114**, 068302 (2015).
- <sup>18</sup>V. N. Biktashev, I. V. Biktasheva, and N. A. Sarvazyan, “Evolution of spiral and scroll waves of excitation in a mathematical model of ischaemic border zone,” *PLoS One* **6**, e24388 (2011).
- <sup>19</sup>F. H. Fenton, E. M. Cherry, H. M. Hastings, and S. J. Evans, “Multiple mechanisms of spiral wave breakup in a model of cardiac electrical activity,” *Chaos* **12**, 852–892 (2002).
- <sup>20</sup>V. Biktashev, A. Holden, and H. Zhang, “Tension of organizing filaments of scroll waves,” *Philosophical Transactions of the Royal Society of London. Series A: Physical and Engineering Sciences* **347**, 611–630 (1994).
- <sup>21</sup>H. Zhang and A. Holden, “Chaotic meander of spiral waves in the FitzHugh-Nagumo system,” *Chaos, Solitons & Fractals* **5**, 661–670 (1995).
- <sup>22</sup>D. Barkley, M. Kness, and L. S. Tuckerman, “Spiral wave dynamics in a simple model of excitable media: Transition from simple to compound rotation,” *Phys. Rev. A* **42**, 2489–2492 (1990).
- <sup>23</sup>W. Jahnke, W. E. Skaggs, and A. T. Winfree, “Chemical vortex dynamics in the Belousov-Zhabotinskii reaction and in the two-variable Oregonator model,” *J. Phys. Chem.* **93**, 740–749 (1989).
- <sup>24</sup>F. Fenton and A. Karma, “Vortex dynamics in three-dimensional continuous myocardium with fiber rotation: Filament instability and fibrillation,” *Chaos* **8**, 20–47 (1998).
- <sup>25</sup>C. Henze, E. Lugosi, and A. Winfree, “Helical organizing centers in excitable media,” *Canadian Journal of Physics* **68**, 683–710 (1990).
- <sup>26</sup>R. A. Gray, A. M. Pertsov, and J. Jalife, “Spatial and temporal organization during cardiac fibrillation,” *Nature* **392**, 75–78 (1998).
- <sup>27</sup>A. J. Foulkes and V. N. Biktashev, “Riding a spiral wave: Numerical simulation of spiral waves in a comoving frame of reference,” *Phys. Rev. E* **81**, 046702 (2010).
- <sup>28</sup>M. Bär, N. Gottschalk, M. Eiswirth, and G. Ertl, “Spiral waves in a surface reaction: model calculations,” *The Journal of chemical physics* **100**, 1202–1214 (1994).
- <sup>29</sup>J. Beaumont, N. Davidenko, J. M. Davidenko, and J. Jalife, “Spiral waves in two-dimensional models of ventricular muscle: formation of a stationary core,” *Biophysical Journal* **75**, 1–14 (1998).
- <sup>30</sup>W. Jahnke and A. T. Winfree, “A survey of spiral-wave behaviors in the Oregonator model,” *International Journal of Bifurcation and Chaos* **1**, 445–466 (1991).
- <sup>31</sup>I. S. Aranson and L. Kramer, “The world of the complex Ginzburg-Landau equation,” *Rev. Mod. Phys.* **74**, 99–143 (2002).
- <sup>32</sup>A. N. Iyer and R. A. Gray, “An experimentalist’s approach to accurate localization of phase singularities during reentry,” *Annals Biomed. Eng.* **29**, 47–59 (2001).
- <sup>33</sup>E. M. Annoni, S. P. Arunachalam, S. Kapa, S. K. Mulpuru, P. A. Friedman, and E. G. Tolkacheva, “Novel quantitative analytical approaches for rotor identification and associated implications

- for mapping,” IEEE Transactions on Biomedical Engineering **65**, 273–281 (2018).
- <sup>34</sup>T.-C. Li, D.-B. Pan, K. Zhou, R. Jiang, C. Jiang, B. Zheng, and H. Zhang, “Jacobian-determinant method of identifying phase singularity during reentry,” Phys. Rev. E **98**, 062405 (2018).
- <sup>35</sup>C. D. Marcotte and R. O. Grigoriev, “Dynamical mechanism of atrial fibrillation: A topological approach,” Chaos: An Interdisciplinary Journal of Nonlinear Science **27**, 093936 (2017).
- <sup>36</sup>D. R. Gurevich, C. Herndon, I. Uzelac, F. H. Fenton, and R. O. Grigoriev, “Level-set method for robust analysis of optical mapping recordings of fibrillation,” Computing in Cardiology **44**, 1 (2017).
- <sup>37</sup>A. Karma, “Spiral breakup in model equations of action-potential propagation in cardiac tissue,” Phys. Rev. Lett. **71**, 1103–1106 (1993).
- <sup>38</sup>A. Karma, “Electrical alternans and spiral wave breakup in cardiac tissue,” Chaos **4**, 461–472 (1994).
- <sup>39</sup>C. C. Mitchell and D. G. Schaeffer, “A two-current model for the dynamics of cardiac membrane,” Bulletin of Mathematical Biology **65**, 767–793 (2003).
- <sup>40</sup>C. R. Maurer, R. Qi, and V. Raghavan, “A linear time algorithm for computing exact Euclidean distance transforms of binary images in arbitrary dimensions,” IEEE Transactions on Pattern Analysis and Machine Intelligence **25**, 265–270 (2003).
- <sup>41</sup>D. Schwarz, “Fast and Robust Curve Intersections,” <http://www.mathworks.com/matlabcentral/fileexchange/11837-fast-and-robust-curve-intersections>.
- <sup>42</sup>D. Blair and E. Dufresne, “The Matlab Particle Tracking Code Repository,” <http://site.physics.georgetown.edu/matlab/index.html>.
- <sup>43</sup>J. C. Crocker and D. G. Grier, “Methods of digital video microscopy for colloidal studies,” Journal of colloid and interface science **179**, 298–310 (1996).
- <sup>44</sup>H. Ashikaga, Private communication.

## Appendix A: Parameter sets

For the reference analysis, the parameters used were  $MPP_1 = 0.01$ ,  $MPP_2 = 0.05$ ,  $\delta = 0.2$ ,  $\sigma_s = \sigma_t = 0$  (no initial smoothing), and  $\sigma_d = 4$ . For the noisy/sparse data,  $\sigma_t$  was changed to 5 and the minimum peak prominences depended on the noise as indicated in Table IV.

	$\eta = 0$	$\eta = 0.1$	$\eta = 0.3$	$\eta = 1$
$MPP_1$	0.01	0.05	0.25	0.25
$MPP_2$	0.05	0.1	0.25	0.25

TABLE IV. Minimum peak prominences used for different levels of noise  $\eta$ .